J MATER SCI **41** (2006) 2749–2759

Review

Effects of supercooling and cooling rate on the microstructure of Cu–Co–Fe alloys

A. MUNITZ*
Nuclear Research Center-Negev, P.O.Box 9001, Beer-Sheva, Israel

A. M. BAMBERGER
Materials Science and Engineering, Technion, Technion City, Haifa, Israel

S. WANNAPARHUN
Department of Materials Science and Engineering, University of Florida, Gainesville, Florida 32611, USA

R. ABBASCHIAN
College of Engineering, University of California, Riverside, CA 92521

The effects of supercooling and cooling rate on the microstructure of ternary Cu–Fe–Co alloys were investigated. Electromagnetic levitation was used to supercool the liquids down by 180 K. Alloys with 11 at.% Cu and less than 19 at.% Fe contained fcc (Fe, Co) and fcc Cu phases; those with 19 to 23 at.% Fe contained bcc (Fe, Co), fcc (Fe, Co) and fcc Cu; those with more than 23 at.% Fe contained bcc (Fe, Co) and fcc Cu. The primary dendrites contained 10 to 20 at.% Cu, with Fe and Co contents depending on the alloy composition. Supercooling the melt below a certain temperature resulted in metastable separation of the melt into two liquids, one (Co + Fe)-rich, the other Cu-rich. The metastable phase separation temperatures and the two liquid compositions were determined experimentaly, and compared with calculated ones. Isothermal cross-sections at various temperatures were constructed for stable and metastable cases based on thermodynamic and experimental data of the Cu–Co, Cu–Fe, and Co–Fe systems. A peritectic reaction for the ternary alloys was found at approximately 1100°C.

---

1. Introduction

Since the last decade, there is an increased interest in materials exhibiting giant magneto resistance (GMR) [1, 2], where a relatively large drop in the electrical resistance is observed under a magnetic field. Cu–Co alloys exhibit such GMR [1, 2]. For example, a supersaturated $Cu_{90}Co_{10}$ solid solution exhibited a magnetoresistance ratio of 11% at room temperature after annealing at 440°C. It has been suggested, that enhancement of the GMR ratio in that material is related to fine Co precipitates resulting from solid-state spinodal decomposion of the supersaturated alloy [1, 2].

Previous studies revealed that supercooling of Cu–Fe, Cu–Co, and Cu–Fe–Co alloys beyond a certain limit resulted in metastable liquid phase separation, where the supercooled liquid was separated into two liquids, Cu-rich (L2), and Co or Fe-rich (L1) [3, 4–10]. The separation boundaries for Cu–Co and Cu–Fe systems were consistent with theoretical thermodynamic calculations [11–15]. Isothermal sections for ternary Cu–Co–Fe alloys were constructed [16] based on the Fe–Cu [11, 12] and Co–Cu [12, 15] phase diagrams, and some thermodynamic data such as melting temperatures [17]. The solidus and liquidus temperatures as well as the metastable miscibility gap for Cu–Co–Fe were calculated according to a modified database [18]· There is, however, no information on stable and metastable Cu–Co–Fe ternary diagrams at room temperature. This work is

---

*Author to whom all correspondence should be addressed.

0022-2461 © *2006 Springer Science + Business Media, Inc.*
DOI: 10.1007/s10853-006-5598-8

aimed at investigating the effects of supercooling and cooling rate on the formation of stable and metastable phases in Cu–Fe–Co ternary alloys.

2. Experimental procedures

2.1. Specimen preparation

High purity copper (99.98%), cobalt (99.99%), and iron (99.99%) were used to prepare Cu–Co–Fe alloys containing up to 85 at.% Cu. The raw materials were weighed with an accuracy of ±0.01 g to prepare samples with compositions ranging from 5 to 96 at.% Cu, 2 to 80 at.% Co and 2 to 85 at.% Fe. Three combinations of specimen melting and solidifying techniques were used: arc melting, induction melting, and levitation melting. They are described below.

For arc melting, specimens approximately 25-g each were melted using a non-consumable tungsten electrode. Several remelting cycles were performed, and the specimens were turned over before each remelting to ensure homogeneity. The cooling rates entailing this technique are approximately 10 K/s. The designations of the arc melted samples and their compositions are given in Table I. The solidified specimens were used for microstructural characterization. The induction melted samples, approximately 15-g each, were melted in an alumina crucible placed inside a graphite susceptor. The temperature was raised above 1600°C for approximately 30 min. to homogenize the melt. The liquid was then cooled down to 1000°C at a rate of approximately 3×10^{-2} K/s, then allowed to cool rapidly to room temperature in the furnace ambient. These samples were used for X-ray analysis. Finally, for electromagnetic levitation, the specimens listed in Table II, weighing approximately 1.5 g each, were arc melted and then levitated using an electromagnetic (EM) levitation apparatus described elsewhere [19, 20]. The temperature of the levitated specimens was continuously monitored using a two-color optical pyrometer equipped with a data acquisition system. A typical thermal cycle during levitation consisted of repeated melting, superheating by about 200 K, than cooling. In general, an adjustable flow of a He/Ar gas mixture passed the levitated samples controlled the heating and cooling cycles. Some samples solidified while levitated, at cooling rates of around 100 to 200 K/s. Other samples were quenched on a copper chill, from the drop temperature T_{drop}, starting with the following initial states: (i) superheated liquid (ii) solid/liquid mixture (iii) supercooled liquid.

2.2. Microstructural characterization

The specimens were cross-sectioned, polished, and subsequently etched for 5–12 s using a solution of 10 g ammonium cupric chloride and and ammonium hydroxide sufficient for dissolving all the ammonium chloride crystals in 120-ml of distilled water. For EDS analysis, the specimens were etched lightly to reveal the microstructure while keeping the surface roughness to a minimum. The composition data were corrected using energy dispersive spectroscopy equipped with a standard ZAF program [21]. The accuracy of the EDS was confirmed by comparing the results to those measured using wavelength dispersive spectroscopy (WDS), using pure Cu, Co, and Fe as standards. The two methods agree by better than 0.3 at.%

X-ray diffraction characterization of the polished but unetched specimens was done using 40-kV, 40-mA Cu-Kα radiation. The scan speed was 0.5 degrees per minute, and Silicon calibration was carried out for Si with EXECAL [22]. The cell parameters of each phase were then calculated using a 2θ least square program [23].

2.3. Thermodynamic calculations

Initial thermodynamic calculations of the ternary alloys were performed using the database reported in [18]. It was found, however, that contrary to experiment, the calculations resulted in a stable liquid phase separation region for some compositions. Therefore, the database was modified so as to eliminate the stable liquid phase separation region while having no effect on the calculated phase boundaries of the binary-edge diagrams. This was accomplished by adding a small ternary correction term to both the fcc and liquid phases given by the following equation [18]

$$^{E}G^{L}(\text{ternary}) = x_{Co}x_{Cu}x_{Fe}$$
$$((5000x_{Co} - 80000x_{Cu} + 10000x_{Fe}),$$

where$^{E}G^{L}$ (ternary) is the excess Gibbs energy x_{Co}, x_{Cu} and x_{Fe} are the mol fractions of Co, Cu and Fe, respectively. This modified free energy equation was then used to calculate the metastable liquid immiscibility phase boundaries during melt supercooling. The isothermal cross-section at 25°C of the stable Cu–Co–Fe phase diagram was also calculated, together with the composition and fraction of the liquid and the peritectic temperatures using Scheil's segregation model.

3. Results

3.1. Microstructures

Secondary electron (SE) images of the arc melted ternary of Cu–Co–Fe alloys with different Co+Fe contents are shown in Fig. 1. In general, the microstructures consisted of primary (Fe, Co) rich dendrites surrounded by a Cu-rich matrix. As will be shown in Section 3.4, up to three phases; bcc (Fe, Co), fcc (Fe, Co), and fcc Cu were present, depending on the alloy composition. The primary dendrite exhibited the normal structure, with prepedicular branching. However, in some locations, such as the one shown in Fig. 1a, the dendrite branches appeared to be 60° apart. Usually, such behavior indicates the presence of an hcp structure. On the other hand, X-ray analysis of the cooled samples showed no presence of any hcp phase. It is thus likely that these dendrites grow in $\langle 110 \rangle$ directions; this point has not been studied further.

The detailed microstructure of the matrix, shown in Fig. 2, was similar to the peritectic microstructure observed in binary Cu–Co and Cu–Fe systems. At low Co + Fe contents (below 20 at.%), the matrix consisted of

TABLE I Summary of the microprobe analysis of average alloy composition, dendrite composition, and interdendritic composition for arc-melted specimens used for microstructural examinations.

	Average alloy composition			Average dendrite composition			Average interdendrite composition		
Alloy No.	Cu (at.%)	Co (at.%)	Fe (at.%)	Cu (at.%)	Co (at.%)	Fe (at.%)	Cu (at.%)	Co (at.%)	Fe (at.%)
1	5.5	10.4	84.1	Grained structure			Grained structure		
2	9.4	12.0	78.6	9.3	12.1	78.6	90.7	1.5	7.8
3	10.2	78.7	11.1	14.7	74.7	10.5	90.4	7.6	2.0
4	10.7	68.5	20.7	10.3	68.7	21.0	90.1	7.9	2.0
5	12.4	71.9	15.7	13.9	70.3	15.8	90.5	7.8	1.7
6	20.4	29.6	50	11.9	32.9	55.1	92.4	3.3	4.4
7	36.6	31.4	32	12.1	43.7	44.7	93.0	3.6	3.4
8	36.2	11.0	52.8	11.2	15.7	73.1	88.0	2.7	9.3
9	54	22	24	15.5	40.6	43.9	92.1	3.8	4.1
10	56	14	30	20.0	25.3	54.7	95.5	3.2	5.5
11	63	26	11	17.8	56.9	25.2	92.0	5.1	2.9
12	68.5	23.3	8.2	16.9	53.8	29.3	95.5	2.7	1.8
13	74	18	8	19.6	54.6	25.8	89.7	7.6	2.7
14	77	11	12	16.7	39.3	44.0	91.4	4.4	4.2
15	80.4	5.8	13.8	14.6	27.2	58.2	91.5	2.6	5.9
16	89	6	5	17.0	43.0	40.0	93.2	3.9	2.9

Cu-rich dendrites, with a bright region near the primary Co + Fe dendrites, and a dark region away from them as shown in Figs 1a and b, respectively. In addition, a morphological change of the interdendritic phase for alloys containing more than 30 at.% Co + Fe was observed from the peritectic (Figs 1a and b) to the one shown in Fig. 1d. Specimens prepared in the induction furnace had a similar microstructure, yet coarser than that of the arc-melted ones.

The EDS analysis showed that the dendrites contained approximately 10–20 at.% Cu, with the balance Co+Fe content, as summarized in Table I. Moreover, the Fe and Co contents in the dendrites were proportional to the nominal composition of the original melt. The same tendency was also observed for the average interdendritic composition. The elemental analysis of the Cu phase surrounding the (Fe, Co) dendrites (Figs 1a and b and 2) indicated that the color contrast was due to a compositional gradient. A summary of the average composition of the Cu-phase, the center, and the periphery of the Cu dendrite for two Cu–Co–Fe alloys are given In Table III.

3.2. Supercooling effects on the microstructure

A typical microstructure of Cu–Co–Fe alloys solidified with only small supercooling is shown in Fig. 3. Similar to Cu–Co–Fe alloys solidified at slow cooling rates, the appearance of Co + Fe denrites (bright areas in the figure) is followed by the peritectic reaction of the Cu-phase. Since cooling rates obtained by this technique were larger than those obtained by arc-melting, the microstructure is finer. The change in the dendritic composition as a function of the original melt composition was similar to that of the dendritic composition under slow cooling rates.

TABLE II Summary of Cu–Co–Fe EM levitation specimen compositions, melting temperatures, and two melt separation temperatures.

	Composition (at.%)			MeltingTemperature (°C)		Separation Temperature—T_{SEP} (°C)	
Alloy No	Cu	Co	Fe	Measured	Calculated	Measured	Calculated
1	95.6	2.1	2.3	1090	1090**		
2	89.0	5.4	5.6	1143	1210*,**		
3	81.6	8.4	10.0	1230	1245	<1140	1110
4	78.3	10.6	11.1	1240	1250**		
5	78.1	5.3	16.6	1300	1310**		
6	72.9	10.5	16.6	1280	1270	1195	1200
7	69.5	5.2	25.3	1315	1350	1270	1250
8	62.9	26.1	11.0	1290	1280	1265	1150
9	57.8	31.2	11.0	1280	1295**		
10	57.5	20.7	21.8	1300	1290	1220	1140
11	52.7	31.0	16.3	1330	1360	1270	
12	52.1	10.2	37.7	1355	1360	1315	1180
13	46.7	16.4	36.9	1340	1360	1260	
14	44.7	36.9	18.4	1325	1330	1270	1130

*Large discrpency between the calculate and measured

**alloy used for measuring melting temperature only.

TABLE III The composition of the different regions in the ε-Cu dendrite arm for two Cu–Co–Fe alloys. The numbers in brackets are the calculated peritec composition.

	Composition measured		
Zone	Cu (at.%)	Co (at.%)	Fe (at.%)
Cu-13.8 at.% Fe-5.8 at.% Co			
Average	95.8 (95.5)	2.8 (3.0)	1.4 (2.5)
Center	94.1	4.1	1.8
Circumference	97.5	1.6	0.9
Cu-8.2 at.% Fe-23.3 Co			
Average	94.4 (93.0)	1.6 (1.0)	4.0 (6.0)
Center	93.6	1.4	5.0
Circumference	97.2	0.8	2.0

For larger Cu–Co–Fe alloy supercooling, the liquids entered a metastable liquid miscibility gap, and separated into two liquids; (Fe+Co) -rich (L1) and Cu-rich (L2). Scanning electron (SE) images of a 50-K supercooled Cu-16 at.% Co-34 at.% Fe in Fig. 4 revealed the microstructure at various locations relative to the chill. Close to the chill (up to 50 μm distance), the microstructure consisted of very fine spherulites embedded in a Cu-matrix (Fig. 4a), turning coarser as the distance increased (Fig. 4b). At 200 μm distance from the chill, a mixed microstructure of spherulites with dendrites was observed (Fig. 4c), with the amount of the dendrites increasing with distance from the chill. At 800 μm distance from the chill, no spherulite, only dendrites were observed (Fig. 4d).

Secondary electron (SE) images of a Cu-16 at.% Co-34 at.% Fe supercooled 140-K and then dropped on a copper chill are shown in Fig. 5. Unlike the specimen shown in Fig. 4, this specimen underwent phase separation before contacting the copper chill. The microstructure consists of dark Co+Fe rich (L1) regions, and bright Cu-rich (L2) ones. The microstructure of the L1 and L2 is shown in Figs 5c and d at larger magnification. The Cu-rich (L2) microstructure is similar to that of Fig. 3. In contrast, the

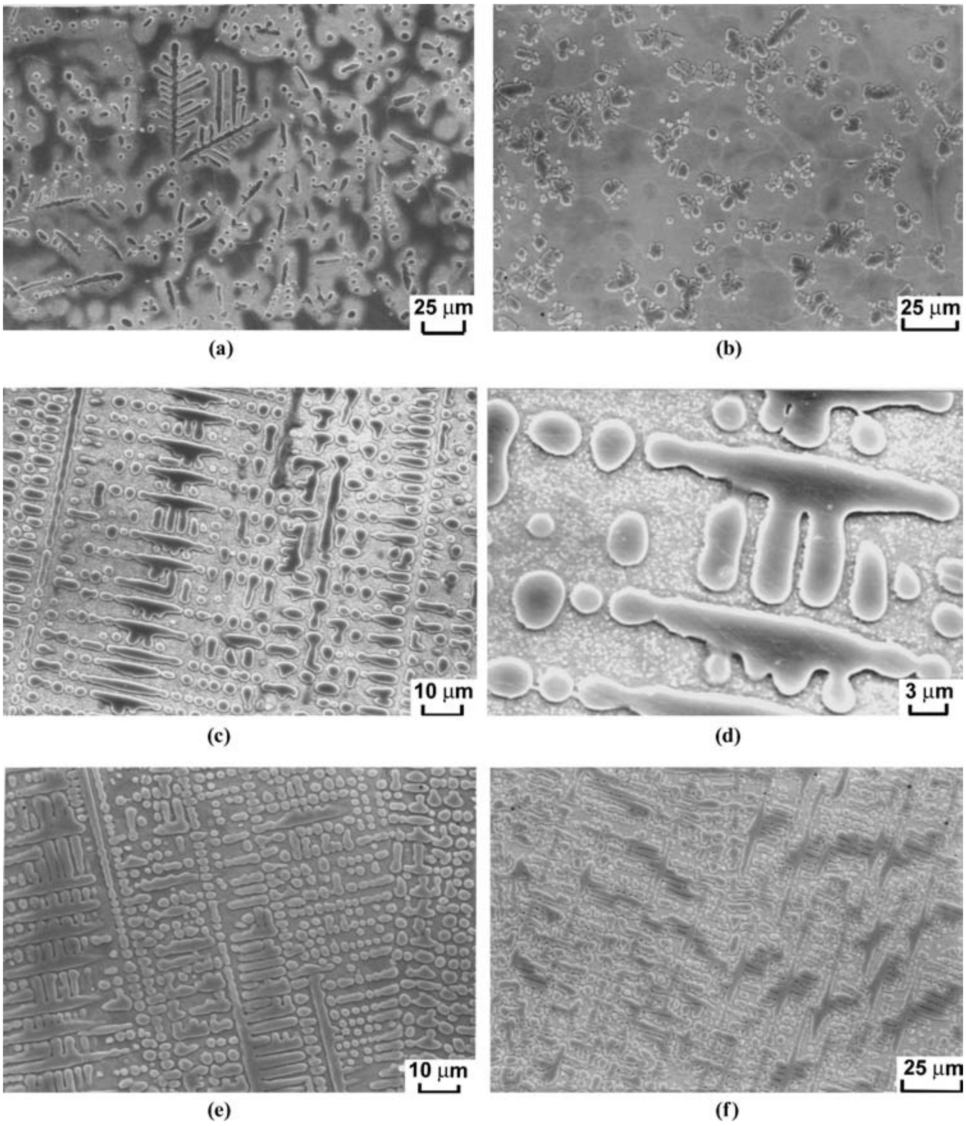

Figure 1 Secondary electron images illustrating the microstructure of arc-melted ternary Cu–Co–Fo alloys. (a) Cu-6 at.% Co-5 at.% Fe. (b) Cu-6 at.% Co-14 at.% Fe. (c, d) Cu-26 at.% Co-11.0 at.% Fe. (e) Cu-14 at.% Co-30 at.% Fe. (f) Cu-31.4 at.% Co-32 at.% Fe.

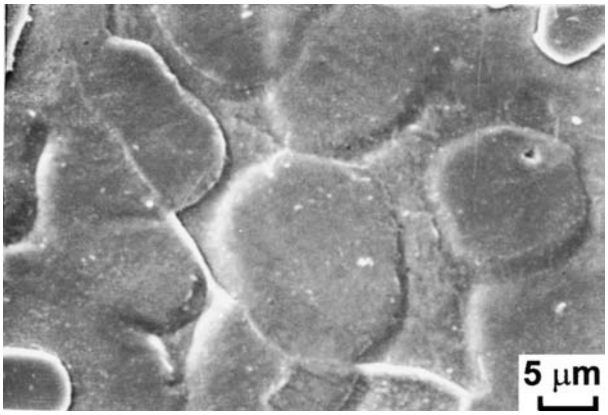

Figure 2 Secondary electron images illustrating the microstructure of peritectic solidification in Cu-13.8 at.% Fe-5.8 at.% Co alloys.

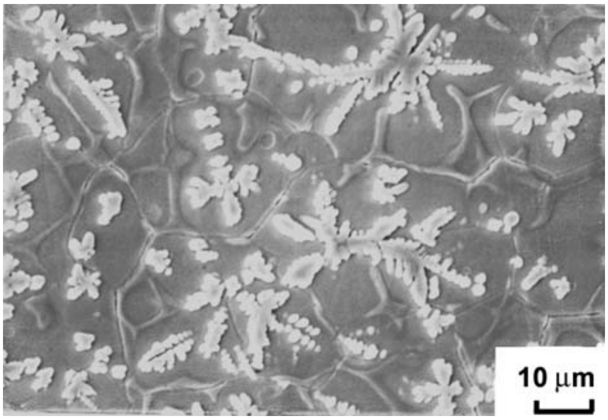

Figure 3 The microstructure of Cu-8 at.% Co-30 at.% Fe Alloy solidified with small supercooling while levitated at a cooling rate of about 100°C/s.

Co+Fe (L1) had a unique non-dendritic morphology, as shown in Fig. 5c. In several cases, the L1 region contained small L2 spheres as shown in Figs 5a and b. As will be discussed later, these spheres represented secondary phase separation within the L1 phase. The overall composition of L1 and L2 were Cu-20 at.% Co -63 at.% Fe and Cu-3 at.% Co-7 at.% Fe, respectively. The compositions of L1 and L2 for the levitated samples measured in the same manner, with the corresponding liquid phase separation temperature, T_{sep}, and actual dropping temperature, T_{drop}, are summarized in Table IV.

The influence of strong electromagnetic stiring on the phase separeted liquids can be seen by comparing the microstructure of two Cu-16 at.% Co-34 at.% Fe specimens shown in Fig. 6. Both samples were dropped on the chill after 180-K supercooling. The sample in Fig. 6b showed recalescence while levitated. The microstructure of the first specimen is similar to that given in Fig. 5. The other sample, however, shows strong swirling flow patterns with a much more complicated microstructure, as shown in Fig. 6b, and in Fig. 7 at a higher magnification.

3.3. X-ray diffraction data

X-ray diffractograms of the alloys solidified under slow cooling rates revealed the presence of three different phases, as shown in Fig. 8. These phases were fcc (Fe, Co), fcc (Cu), and bcc (Fe, Co). The results, summarized in Table V, indicate that for a Cu alloy containing about 11 at.% Cu and less than 19 at.% Fe, the primary dendrites were fcc (Fe,Co) embedded in an fcc Cu phase. For Cu

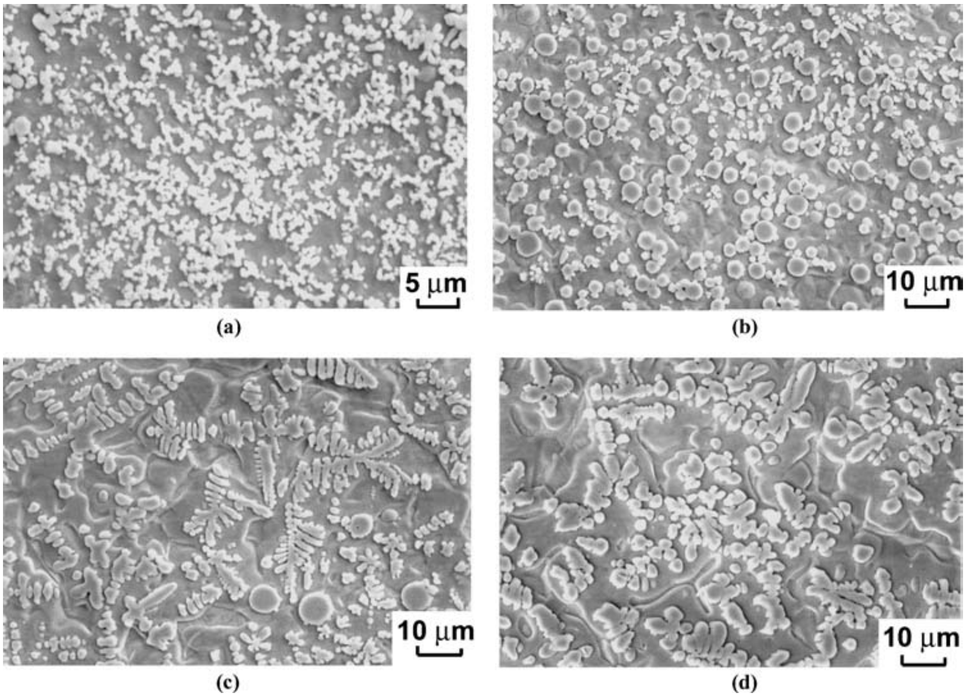

(a) (b) (c) (d)

Figure 4 Secondary electron images illustrating the microstructure of Cu-16 at.% Co-34 at.% Fe dropped on a copper chill after reaching 50 K supercooling at: (a) 10 μm; (b) 50 μm; (c) 200 μm; (d) 800 μm distance from the copper chill.

TABLE IV Summary the L1 and L2 compositions for the different alloys as a function of the supercooling degree.

Alloy composition						L1-Composition			L2-Composition		
Cu (at.%)	Co (at.%)	Fe (at.%)	T_L	T_{SEP}	T_{drop}	Cu (at.%)	Co (at.%)	Fe (at.%)	Cu (at.%)	Co (at.%)	Fe (at.%)
95.6	2.1	2.3	1000		–	No separation			No separation		
89.0	5.4	5.6	1143	∗120<	–	No separation			No separation		
81.6	8.4	10.0	1230		–						
78.3	10.6	11.1	1240		–						
78.1	5.3	16.6	1270		1205						
72.9	10.5	16.6	1280	85	1195	20.8 (7.5)	41.8 (33.5)	37.8 (58.9)	(89.0)	(5.3)	(5.6)
69.5	5.2	25.3	1290	40							
62.9	26.1	11.0	1290	50	1200	20.5 (11.9)	59.3 (48.4)	20.2 (39.6)	81.7 (81.7)	12.7 (12.7)	5.6 (5.6)
					1140	20.5 (11.9)	59.3 (59.6)	20.2 (29.3)	84.9 (83.7)	11.7 (8.5)	3.4 (7.8)
57.5	20.7	21.8	1300	50	1220	22.1 (16.5)	34.8 (39.6)	43.1 (43.9)	82.6 (83.8)	9.6 (11.7)	7.8 (4.5)
					1270	26.2 (21.4)	54.6 (50.1)	19.2 (28.5)	68.1 (82)	24.2 (11.8)	7.7 (6.2)
52.7	31.0	16.3	1330	50	1258	28.1	48.5	23.4	53.0	24.3	22.7
					1180	20.4	52.1	27.5	80.3	6.3	13.4
52.1	10.2	37.7	1355	40	1265	19.2	24.6	23.4	53.0	7.4	16.6
					1175	14.5 (15.4)	18.5 (16.6)	67.0 (68.0)	80.2 (84.6)	4.2 (4.2)	15.6 (11.2)
46.7	16.4	30.9	1340	25	1255	18.2 (13.6)	19.6 (27.5)	62.2 (58.9)	69.2 (83.6)	25.2 (7.4)	5.6 (9.0)
					1200	15.4 (9.1)	19.6 (29.2)	65.0 (61.7)	88.9 (91.2)	3.2 (3.2)	7.9 (5.6)
					1160	23.9 (7.2)	22.8 (29.2)	53.3 (63.6)	77.8 (91.2)	14.5 (3.2)	7.7 (5.6)
44.7	36.9	18.4	1325	70	1240	17.6 (23.3)	53.9 (50.2)	28.5 (26.5)	66.6 (82.7)	11.4 (11.7)	22.0 (5.6)

∗Since T_{SEP} was lower than the temperature achieved no melt separation was observed.

alloys with the same amount of Cu but containing more than 23 at.% Fe, the dendrites consisted of bcc (Fe, Co), and the matrix was fcc Cu. Alloys that contained Fe between 19 and 23 at.% Fe, on the other hand, contained 3 phases; bcc (Fe, Co), fcc (Fe, Co), and fcc Cu.

3.4. Thermodynamic calculations

Three types of calculations were made to determine (i) the isothermal cross section of the stable phase diagram at 25°C, (ii) metastable phase boundaries, and (iii) peritectic reaction in Cu–Co–Fe alloys. The calculated Isothermal cross-section at 25°C, as shown in Fig. 9, revealed the existence two-phase and three-phase regions, as indicated in Table V. However, the calculated three-phase region was predicted to be much larger than that found experimentally. We will consider this difference in section 4 (Discussion).

In order to calculate the metastable phase diagram, the solid phases were excluded, allowing the melt to supercool below its solidus temperature. Then, the temperature in which the supercooled and supersaturated melt decomposed into two liquids was determind. The calculated liquid phase separation temperatures, and the composition of each of the two melts, are summarized in Tables II and IV, respectively. The tables also show the experimental values obtained for the levitated specimens. The two sets of data agree fairly well, the deviation between calculated and measured temperatures being less than 10%. The maximum discrepancy between the calculated and

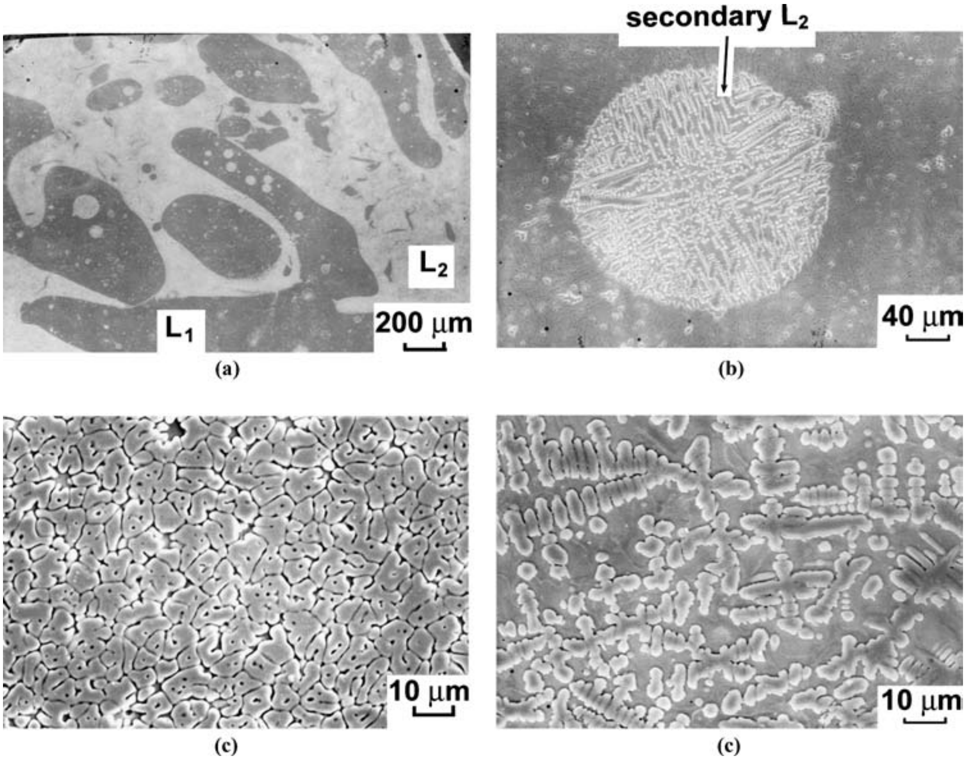

Figure 5 Secondary electron images illustrating the microstructure of Cu-16 at.% Co-34 at.% Fe dropped on a copper chill after 140 K supercooling with recalescnce. (a) an overall view; (b) enlargement of a sphere in (a); (c) microstructure of the Co+Fe rich liquid-L1; (d) microstructure of the Cu rich liquid L2.

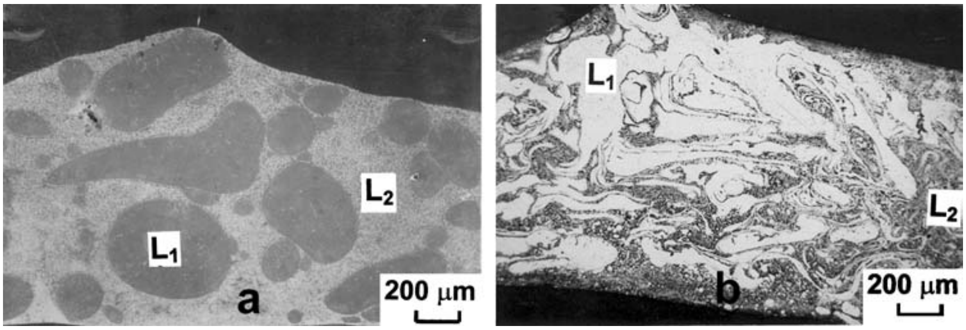

Figure 6 Secondary electron images illustrating the microstructure of Cu-16 at.% Co-34 at.% Fe supercooled to 180 and than quenched onto copper. (a) Dropped prior to recalescence; (b) dropped after recalescence.

TABLE V Summary of the phases found by X-ray diffraction technique.

Alloy no	Coposition Cu (at.%)	Co (at.%)	Fe (at.%)	Microstructure found by X-ray deffraction technique
1	11.2	77.2	11.6	fcc (Fe, Co) + fcc Cu
2	11.1	72.0	16.9	fcc (Fe,Co) + fcc Cu
3	11.1	69.9	19.0	fcc (Fe, Co) + fcc Cu
4	11.1	66.8	22.1	bcc (Fe, Co) + fcc (Fe, Co) + fcc Cu
5	11.1	65.8	23.1	bcc (Fe, Co) + fcc Cu
6	11.1	63.7	25.2	bcc (Fe, Co) + fcc Cu
7	11.0	57.5	31.4	bcc (Fe, Co) + fcc Cu
8	11.0	47.4	41.6	bcc (Fe, Co) + fcc Cu
9	11.0	42.3	46.7	bcc (Fe, Co) + fcc Cu
10	10.9	37.3	51.8	bcc (Fe,Co) + fcc Cu

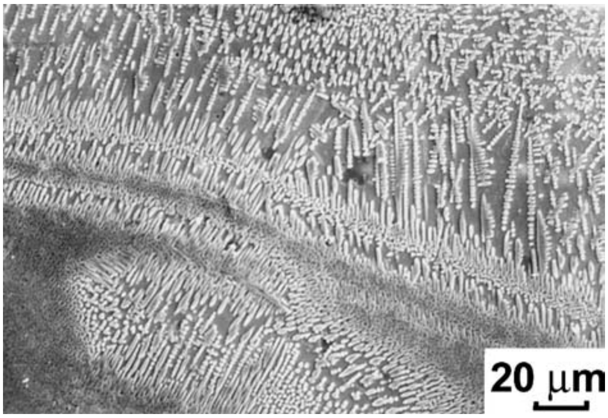

Figure 7 Secondary electron images illustrating the microstructure of Cu-16 at.% Co-34 at.% Fe supercooled 180 K and then quenched onto copper dropped after recalescence.

measured compositions of the major consituent in each liquid is 20%. This point will be discussed later.

The phase formation during normal (non-equilibrium) cooling was calculated using Thermo-Calc. An example of the calculations for Cu-13.8 at.% Fe-5.8 at.% Co alloy is given in Fig. 10. According to it, the first fcc solid forms at 1280°C, with its fraction increasing with a decrease of temperature. At approximately 1100°C, the second fcc solid forms, and and the material consists then of three phases (liquid, fcc(Co, Fe), and fcc-Cu). As temperature drops below 1100°C, the Fe-rich fcc disappears, while the liquid transform into Cu-rich fcc untill solidification terminates. The variation in the calculated melt composition during solidification is shown in Fig. 11. The liquid became Cu-enriched, as the Fe and Co contents decrease due to formation of Co and the Fe-rich fcc phases. The composition of the residual (peritectic) melt at 1100°C was Cu-3 at.% Fe-2.5 at.% Co. The latter value is in good agreement with the experimental results summarized in Table III, the differences between calculations and experiment being less than 1 at.%.

4. Discussion

The microstructures of Cu–Co–Fe alloys solidified without supercooling were similar to that of binary Fe–Cu [5] and Cu–Co [10] alloys. This emerges when one describes

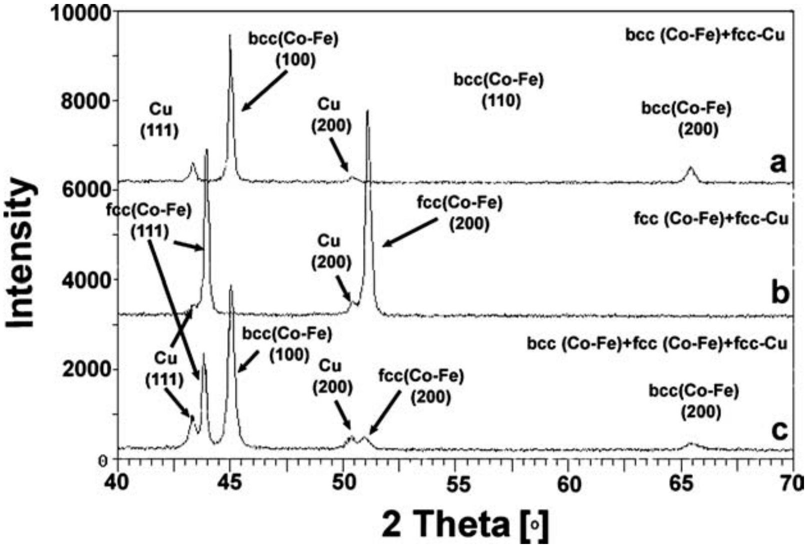

Figure 8 Diffractograms of Cu–Co–Fe alloy exhibited three regions: (a) region of 3 phases: bcc (Co, Fe), fcc (Co, Fe) and fcc-Cu, (b), region of 2 phases: fcc(Co, Fe) and fcc-Cu, and (c) region of 2 phases: bcc (Co, Fe) and fcc-Cu.

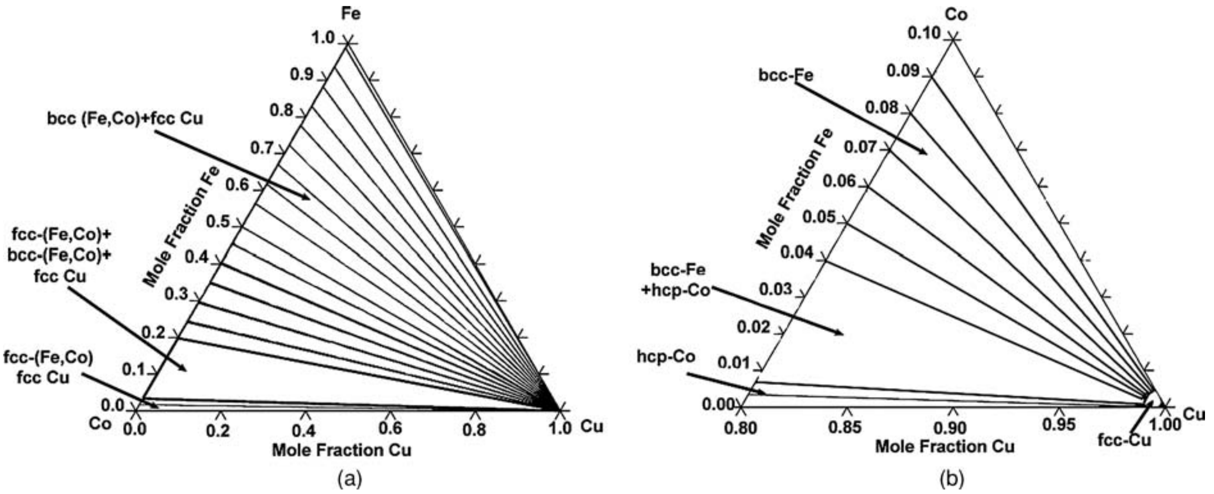

Figure 9 Isothermal cross-section of the Cu–Co–Fe phase diagram at 25°C (a). The Cu rich corner (b).

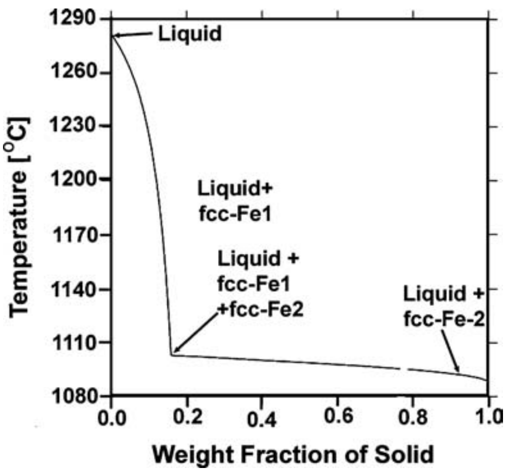

Figure 10 Calculated weight Fraction of solid during solidification of Cu-13.8 at.% Fe-5.8 at.% Co.

the ternary boundary of Cu–Co–Fe as a quasi-binary phase diagram, where one axis represents pure copper, the other representes the Fe+Co binary composition [17]. For example, a liquid with a Co+Fe content of C_0, the primary phase to solidify is expected to be a (Fe, Co) dendrite. The dendritic and liquid compositions then follow the solidus and liquidus lines, respectively, as temperature is lowered. When the temperature decreases further, a peritectic reaction takes place. The latter has also deduced by the thermodynamic calculations (Table III) suggesting the peritectic reaction to be at 1100°C. In addition, the existence of a peritectic reaction was evidenced from the microstructures observed in Figs 2 and 3. The primary dendritic phase lead to the formation of a copper phase via the peritectic reaction. As the reaction continued, the ε-Cu phase grew around the dendrite until the latter was completely surrounded. At this point, the ternary peritectic reaction significantly slowed down, and the remaining liquid solidified dendritically as ε-Cu dendrites according to the solidus and liquidus of the ε-Cu phase. Because of the reverse slope of the solidus and liquidus lines (i.e. partitioning coefficient larger than 1), the center of the ε-Cu dendrite was rich in Co and Fe, while the periphery contained only small amounts of Co or Fe (Table III).

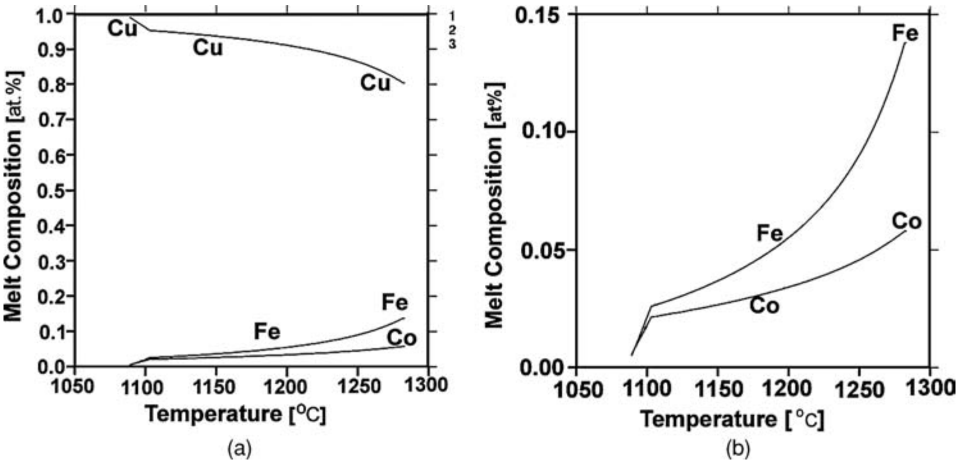

Figure 11 Calculated melt composition as a function of temperature Cu-13.8 at.% Fe-5.8 at.% Co alloy. (a) Overall view. (b) Lower portion of the graph in with more details.

This solidification sequence was obvious in alloys solidified under moderate cooling rates (Fig. 2). The dark region in the center the ε-Cu dendrite element was rich in Fe+Co as compared to the periphery. Similar to the case of the (Fe+Co) dendrite, the ε-Cu dendritic composition also depended on the melt composition (Table III). Moreover, it was found that if the Fe and Co contents in the original melt were equal, the Fe and Co contents in the dendrite were also similar (Table I). It was also possible for Cu-rich dendrites to nucleate and grow in the remaining liquid, especially when the Fe+Co content was less then 10 at.%. For alloys containing more than 20 at.% Fe+Co, the imaging contrast of the ε-Cu dendrites was poor, and a different morphology was observed similar to that in Fig. 1d. It could be suggested, that this type of microstructure was due to a solid-state trasformation resulting in fine (Fe, Co) precipitates. The same type of microstructure was found in the space between ε-Cu dendrites (Figs 1a and b and 2).

As indicated in the perivious section, the ternary boundary of Cu–Co–Fe could be described by a quasi-binary phase diagram, in which one axis represents pure copper and the other represents a pure Fe+Co composition. This simplifies the presentation of the ternary boundaries, as the metastable phase separation surface reduces into a line as in the Cu–Co or Cu–Fe binary systems. The data points for the ternary Cu–Co–Fe liquid phase separation are composed with the phase separation in the binary Cu–Co alloys in Fig. 12. As indicted earlier, the compositions of L1 and L2 were measured using EDS and the T_{drop} was obtained from the thermal history of the levitated samples. In addtion, the metastable liquid phase separation temperatures of the supercooled samples, T_{SEP}, was determind by dropping a series of specimens immediately after recalescence at different supercooling levels. If the microstructure contained spheres, it indicated that the liquid entered the immiscibility gap.

4.1. Impact of supercooling on the microstructure

It should be noted that the solidification path of a phase separated liquid is considerably different and more complicated than that of a supercooled single phase one. This is because each liquid phase not only experiences its own supercooling, which could be considerably different from that of the bulk, but also follows a solidification path that differs considerably from the bulk composition. Moreover, the composition and fraction of each liquid changes as the sample is being continuousely cooled. In general, the composition of each liquid is expected to follow the miscibility phase boundary if adequate time is allowed for the complete transfer of atoms between the two phases. In the absence of such complete diffusion, secondary phase separation of one liquid within the other might occur. An example of this was shown in Fig. 5a.

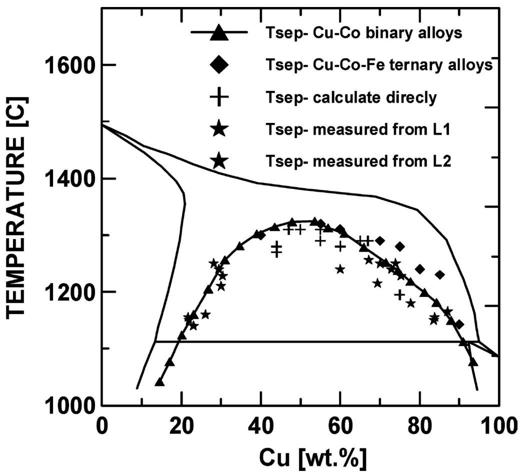

Figure 12 Quasi-binary phase diagram Cu–Co–Fe showing the Liquidus temperature and T_{SEP}, measured by microstructural analysis, as well as EDS composition of L1 and L2 superimposed on the Cu–Co stable phase diagram with Liquid phase separation in Cu–Co melts.

For the present alloys, nucleation depended on the supercooling. The L1 liquid, which is rich in Co and Fe is expected to nucleate and solidify first [9]. However, the heat released by the L1 liquid could raise the temperature above the metastable boundaries, and cause a remix of the separated liquids, if heat removal is not fast enough. As such, the microstructure of the specimen depends not only on the nucleation temperature, but also on the additional supercooling during the free fall, as well as on the cooling rates during solidification. For example, when a Cu–Co–Fe alloy of less than 50 at.% Co+Fe was supercooled into the miscibility gap, melt separation occured. In such a case, the L1 liquid being the minority phase would exhibit spherical shapes embedded in the L2 liquid. There were three possible solidification routes; (i) nucleation prior to dropping, (ii) nucleation during the time interval between dropping and impact on the copper chill (iii) nucleation after impact. In the first case, the latent heat of fusion raised the temperature above the separation temperature, T_{SEP}, resulting in remelting of the first solid, and remixing. The significant convection due to electromagnetic stirring resulted in a swirling pattern of the liquid as shown in Fig. 6b. On the othere hand, when nucleation occurred after releasing from the levitator, large spherical or semi-spherical L1 droplets were obtained, as in Fig. 6a. When nucleation took place after impacting the copper chill, a thin circular specimen with thickness increasing towards the circumference was usually obtained. The high cooling rates during solidification increased the bulk supercooling and also resulted in fine microstructural feathers. Close to the Cu chill, the high cooling rates causes dynamic supercooling, which in turn results in fine spherulites (Fig. 4). Away from the Cu chill, the cooling rate, hence supercooling decreased, and the temperature increased above T_{SEP}, and a regular microstructure was obtained.

As shown in Table II, the measured liquidus and liquid phase separation temperatures and the calculated ones exhibit fair agreement, the largest difference being less than 10%. The measured and calculated composition showed fairly good agreement, particularly with respect to the major component. However, the diagram showed a relatively larger three-phase region than that of the experimental results.

X-ray diffraction measurements showed that for Cu–Co–Fe alloys containing around 11 at.% Cu, and Fe and Co with less than 19 at.% Fe, consisted of a region where two fcc phases, (Fe, Co) and Cu, coexisted. For alloys contained more than 23 at.%, Fe, two-phase bcc (Fe, Co) + fcc Cu were observed. Between 19 and 23 at.% Fe, three-phase bcc (Fe, Co) + fcc (Fe, Co) + fcc Cu were observed. Theoretical calculations indicated (Fig. 11) that the 3-phase region existed between 1 and 20 at.% Fe. The reason for this discrepancy is not clear, and is yet to be investigated. We suspect that the cooling rates used, $\sim 3 \times 10^{-2}$ K/s, are too high for obtaining the stable phase compositions.

5. Summary

The microstructure of Cu–Co–Fe alloys solidified under various supercooling conditions were investigated, yielding the following results:

1. Bulk supercooling of liquids containing 44–80 at.% Cu below a certain temperature, T_{SEP}, resulted in metastable melt separation into two liquids, a Co-rich L1, and a Cu- rich L2. The microstructures of the phase separated specimens consisted of spherulites of one liquid embedded in the other. For alloys containing less than 40 at.% Co+Fe, the spherulites solidified from the L1; those containing more than 50 at.% Co+Fe, the spherulites solidified from the L2.
2. The microstructure of Cu–Co–Fe exhibited a peritectic microstructure, in good agreement with theoretical calculations.
3. Alloys cotaining 11 at.% Cu and more than 72 at.% Co exhibited fcc (Fe, Co) and fcc Cu phases. For less than 65 at.% Co, two-phase bcc (Fe, Co) and fcc Cu coexisted. Between these two regions, a three-phase mixture of bcc (Fe, Co), fcc (Fe, Co) and fcc Cu was observed.
4. The metastable phase boundaries were thermodynamicaly calculated using using the database reported in [18]. The deviation between the calculated values and experimental results was good with the larger discrepencies was less than 10%.

Acknowledgments

The authors thank Dr G. Kimmel and Mr. J. Sariel for their technical assistance with the X-ray diffraction measurements, and Mr. C. Cotler for the microstructural characterization.

References

1. R. BUSCH, F. GARTNER, C. BORCHERS, P. HAASEN and R. BORMANN, *Acta. Mater.* **44** (1996) 2567.
2. J. WECKER, R. VON HELMOLT and L. SCHULTZ, *Appl. Phys, Lett.* **62** (1993) 1985.
3. S. P. ELDER, "Metastable Liquid Immiscibility in Iron-Copper Alloys", Ph.D. Thesis Disertation, University of Florida, 1990.
4. A. MUNITZ, S. P. ELDER and R. ABBASCHIAN, *Met. Trans. A* **23A** (1992) 1817.
5. M. B. ROBINSON, D. LI, T. J. RATHZ and G. WILLIAMS, *J. Mater. Sci.* **34** (1999) 3747.
6. A. MUNITZ and R. ABBASCHIAN, *J. Mater. Sci.* **26** (1991) 6458.
7. C. D. CAO, X. Y. LU and B. B. CHIN, *Phys. Lett.* **15**(11) (1998) 840.
8. D. LI, M. B. ROBINSON, T. J. RATHZ and G. WILLIAMS, *Mater. Lett.* **36** (1998) 152.
9. A. MUNITZ and R. ABBASCHIAN, *J. Mater. Sci.* **33** (1998) 3639.
10. S. P. ELDER, A. MUNITZ and R. ABBASCHIAN, *Materials Sci. Forum* **50** (1989) 137.
11. T. NISHIZAWA and K. ISHIDA, *Bull. Alloy Phase Diagrams* **5** (1984) 61.
12. W. JELLINGHAUS, *Arch. Eisenhutt.* **10** (1936) 115.
13. Y. NAKAGAWA, *Acta Metall.* **6** (1958) 704.
14. Y. Y. CHUANG, R. SCHMID and Y. A. CHAN, *Metall. Tran.* **A15** (1984) 1921.
15. W. R. MADDOCKS and G. E. CLAUSSEN, *Iron and Steel Institute Special Report No.* **14** (1936) 116.
16. In: PhaseDiagrams of Ternary Iron Alloys, Part 6, Indian Institute of Metals, Calcutta, India p 597–599.
17. D. I. KIM and R. ABBASCHIAN, *J. Phase Equilibria* **21** (2000) 1.
18. M. BAMBERGER, A. MUNITZ, L. KAUFMAN and R. ABBASCHIAN, *CALPAD* **26** (2002) 375.
19. A. MUNITZ and R. ABBASCHIAN, in "Undercooled Alloy phases"' C. C. Koch and E. W. Collings, eds. TMS-AIME, Warrendale, Pa, (1987), p. 23.
20. G. J. ABBASCHIAN and M. C. FLEMINGS, *Metal. Trans. A* **14A** (1983) 1147.
21. S. J. B. REED, "Electron Microprobe Analysis", (Cambridge University Press, Cambridge, 1977), pp. 175–197.
22. H. P. KLUG and L. E. ALEXANDER, X-ray Diffraction Procedures for Polycrystalline and Amorphous Materials, 2nd Ed, (Wiley, New York, 1974).
23. D. WILES and R. A. YOUNG, *J. Appl. Cryst.* **14** (1981) 149.

Received 17 November 2004
and accepted 25 July 2005